Exfoliated Graphene into Highly Ordered Mesoporous Titania Films: Highly Performing Nanocomposites from Integrated Processing

Luca Malfatti,*,[†] Paolo Falcaro,[‡] Alessandra Pinna,[†] Barbara Lasio,[†] Maria F. Casula,[§] Danilo Loche,[§] Andrea Falqui,[⊥] Benedetta Marmiroli,[‖] Heinz Amenitsch,[‖] Roberta Sanna,[#] Alberto Mariani,[#] and Plinio Innocenzi*,[†]

[†]Laboratorio di Scienza dei Materiali e Nanotecnologie, CR-INSTM, Università di Sassari, Palazzo Pou Salid, Piazza Duomo 6, 07041 Alghero (SS), Italy

[‡]Division of Materials Science and Engineering, CSIRO, Clayton South, MDC 3169 Australia

[§]Dipartimento di Scienze Chimiche e Geologiche Università di Cagliari, 09042 Monserrato (CA), Italy

[⊥]Istituto Italiano di Tecnologia, IIT, Via Morego 30, 16163 Genova, Italy

[‖]Institute of Inorganic Chemistry, Graz University of Technology, Stremayrgasse 9/IV 8010 Graz, Austria

[#]Dipartimento di Chimica e Farmacia, Università di Sassari, Via Vienna 2, 07100 Sassari, Italy

Ⓢ *Supporting Information*
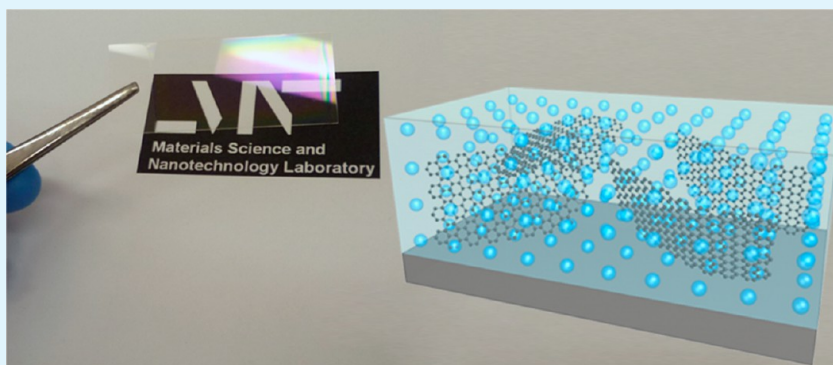
ABSTRACT: To fully exploit the potential of self-assembly in a single step, we have designed an integrated process to obtain mesoporous graphene nanocomposite films. The synthesis allows incorporating graphene sheets with a small number of defects into highly ordered and transparent mesoporous titania films. The careful design of the porous matrix at the mesoscale ensures the highest diffusivity in the films. These exhibit an enhanced photocatalytic efficiency, while the high order of the mesoporosity is not affected by the insertion of the graphene sheets and is well-preserved after a controlled thermal treatment. In addition, we have proven that the nanocomposite films can be easily processed by deep X-ray lithography to produce functional arrays.

KEYWORDS: mesoporous materials, patterning, titania, exfoliated graphene, thin films

INTRODUCTION

Carbon-based nanostructures, such as nanotubes and graphene sheets, significantly improve the functional properties of hybrid organic-semiconductor nanocomposites due to their extraordinary electron mobility.[1,2] Graphene—titania nanomaterials, for example, are of paramount interest because of their electrical,[3−5] mechanical,[6] sensing,[7,8] photovoltaic,[9−11] and photocatalytic properties.[12−14] The coupling between graphene and titanium dioxide allows enhancing the photocatalytic mechanism of nanocomposite powders and coatings because, if compared to pure titania, the nanocomposite reduces the probability of photoinduced electron and hole recombination.[15]

In this context, a few attempts on combining these functional materials have raised the potential and the limitations of titania/graphene nanocomposites. For instance, thick films made by a graphene scaffold filled with titania nanoparticles showed very high photocatalytic efficiency; however, the films were completely opaque to visible light.[11] On the contrary, thin films did not present any improved functional properties when doped with graphene.[16] Du et al. faced an additional problem: although the successful combination of graphene oxide and porous titania was achieved, however, the low accessibility of the porosity prevented an efficient photocatalytic property. The authors addressed this problem using a second templating agent (polystyrene nanoparticles) to improve the pore accessibility. With this strategy, the new thick hierarchical

graphene-doped TiO_2 nanocomposite coating presented better photocatalytic properties when compared with the pure TiO_2 system. Unfortunately, the combination of big pores and thick films drastically compromises the optical transparency. Although these pioneering studies on TiO_2/graphene coatings presented interesting perspectives, a fabrication method which allows fully exploiting the technological advantages of a TiO_2/graphene coating is still missing.

To fill this gap, we have carefully designed a combination of exfoliated graphene (EG) and highly ordered porous titania enabling the fabrication of a thin film with enhanced properties. The porous architecture has been designed to ensure the highest diffusivity in the films, while the use of highly dispersed EG has allowed maximizing the nanocomposite properties.

Another technological challenge we have faced is the possibility to integrate the deposition of films from liquid phase (bottom-up approach) with a specific patterning technique (top-down route) such as deep X-ray lithography (DXRL); in fact, for many industrial applications, it is preferable to write micrometer-sized patterns or arrays on TiO_2 films.[17] Although DXRL is not largely diffusive for industrial applications compared to other fabrication processes, our integrated approach allows for the selective densification of the inorganic matrix and simultaneous removal of the templating agent from the organized porous structure.[18]

■ EXPERIMENTAL SECTION

1-Vinyl-2-pyrrolidone (NVP, Sigma-Aldrich), graphite (Sigma-Aldrich), titanium tetrachloride ($TiCl_4$, Aldrich), triblock copolymer Pluronic F127 ($OH(CH_2-CH_2O)_{106}-(CHCH_3CH_2O)_{70}(CH_2CH_2-O)_{106}$, Sigma), ethanol (EtOH, Fluka), distilled water, and stearic acid (Fluka) were used as received without further purification. p-Type/boron-doped, (100)-oriented, 400 μm thick silicon wafers (Si-Mat) and 1.2 mm thick silica slides (UV grade from Heraeus) were used as substrates.

Sol Preparation. A graphene batch solution was prepared by dispersing 5 wt % graphite flakes in NVP, placing into a tubular plastic reactor (inner diameter 15 mm), and ultrasonicating it for 24 h at 25 °C (ultrasound bath EMMEGI, 0.55 kW). Then, the dispersion was centrifuged for 30 min at 4000 rpm, and the gray to black liquid phase containing graphene was recovered. The concentration of the graphene dispersion, obtained by gravimetric filtration through polyvinylidene fluoride filters (pore size 0.22 mm), was 2.27 mg mL^{-1}. The precursor sol for the deposition of nanocomposite titania films was prepared by adding dropwise 1.1 mL of $TiCl_4$ into a mixture of 23.4 mL of EtOH and 0.65 g of Pluronic F127. After the mixture was stirred for 15 min at room temperature, 1.8 mL of distilled water was added. The molar ratio of the reagents in the film solution was $TiCl_4/EtOH/F127/H_2O = 1:40:0.005:10$. As a final step, increasing amounts of graphene dispersion were added to 2 mL of precursor sol in a volume range from 0 up to 200 μL, and the mixture was left under stirring for other 10 min before film deposition.

Material Synthesis. Nanocomposite titania thin and thick films were prepared by both dip- and spin-coating. For dip-coating, the substrates were immersed in the titania–graphene sol and then withdrawn with a rate of 15 cm min^{-1} at relative humidity (RH) of 30%. For spin-coating, 50 μL of solution was cast on 2 × 2 cm^2 monocrystalline silicon wafers and fused silica substrates at 30% RH. The amount of revolutions per minute was set at 3000 rpm for 40 s followed by 300 rpm for 30 s. Coatings with increased thickness were prepared by decreasing the revolutions per minute from 3000 down to 300 rpm. A table resuming the difference among the samples used for characterizations (graphene dispersion volumetric fraction, thermal treatment, film thickness, and type of substrate) is reported in the Supporting Information as Table ST1.

Patterning Process. After deposition, the nanocomposite films were directly exposed to hard X-rays using the deep X-ray lithography

beamline at Elettra synchrotron facility (Trieste, Italy). Hard X-rays were obtained from the storage ring working at 2 GeV with a white beam of energy ranging from 2 to 20 keV. The beam shape can be found at the Elettra Web site.[19] The films characterized by FTIR spectroscopy were irradiated with increasing X-ray doses, without lithographic mask, by changing the exposure time. The energies per unit area incident to the sample surface were 275, 550, 1100, and 2200 J cm^{-2}. The sample for Raman mapping was irradiated with 1100 J cm^{-2} through a test mask. During X-ray exposure, the samples were mounted on the top of a water-cooled stainless steel plate (scanner), which was kept in continuous motion to obtain a homogeneous exposure of areas larger than the beam size; the scanner rate was set to 20 mm s^{-1}. After exposure, the samples were dipped in ethanol for around 30 s, rinsed in isopropyl alcohol for 15 s, and finally dried with a flow of nitrogen to avoid remaining residuals.

Thermal Treatment. In order to check the photocatalytic properties, the samples were first treated in oven at 100 °C for 12 h and then fired in a tubular reactor with an argon flux (50 mL min^{-1}) with the following heating ramp: from room temperature up to 400 °C with a rate of 10 °C min^{-1}, 3 h at 400 °C, heating up to 450 °C with a rate of 5 °C min^{-1}, 2 h at 450 °C.[16] After this time, the furnace was turned off so that the samples were slowly cooled to room temperature.

Material Characterization. Samples were observed at different magnifications by an optical microscope Nikon Optiphot 500 and using secondary electron (SE) scanning electron microscopy (SEM) by a JEOL JSM-7500FA microscope, equipped with a cold field emission electron gun and operating at 5 kV.

A Bruker Senterra confocal Raman microscope working with a laser excitation wavelength of 532 nm at 5 mW of nominal power was used for Raman characterization. Raman mapping was obtained with a 10× objective, and an array of 60 × 30 points was defined to cover an area of 120 × 60 μm^2 with a step of 2 μm. Each spectrum of the map was obtained by averaging five acquisitions of 4 s.

Fourier transform infrared (FTIR) measurements were obtained by using a Vertex 70 Bruker spectrophotometer equipped with a RT-DTGS detector and a KBr beam splitter. The spectra were recorded in the 400–4000 cm^{-1} range with a resolution of 4 cm^{-1} using a silicon wafer as the background reference. The baseline was corrected using a concave rubber-band method (OPUS 6.5 software) using 64 baseline points and one iteration.

Transmission electron microscopy (TEM) images were obtained by using an Hitachi H-70000 microscope equipped with a tungsten cathode operating at 125 kV and a JEOL JEM 1011 microscope, equipped with a field emission electron gun and a spherical aberration corrector and operating at 100 kV. Two different sample preparations were used depending on the type of measurement. For general measurements, fragments obtained by scratching the films were dispersed in ethanol by ultrasonication and then dropped on a carbon-coated copper grid and dried for observations. The (101) diffracted beam was imaged for the dark-field analysis. For cross-section measurements, two small plates were prepared by cutting the sample at a fixed height of the substrate. A rough mechanical polishing procedure was carried out on all the samples to achieve around 50 μm in thickness. The polishing for the cross-section sample was performed in the direction parallel to the substrate cut, while polishing for the planar view sample was performed in the direction perpendicular to the substrate cut. Final thinning to reach electron transparency was achieved by precision ion milling with a JEOL IS (Ion Slicer).

The organization of the porous structure was investigated by 2D grazing incidence small-angle X-ray scattering (GISAXS)[20,21] at the Austrian SAXS beamline at Elettra.[22,23] The incident energy was set at 8 keV (λ = 1.54 Å). The incident angle of the beam was set at 0.5 ± 0.1° to obtain the highest contrast between the GISAXS pattern and the background. A 2D CCD detector was used to acquire the scattering patterns.

X-ray diffraction (XRD) patterns of nanocomposite and pure titania films were collected with a Bruker D8 Discover instrument working in grazing incidence geometry with a Cu Kα line (λ = 1.54056 Å); the X-ray generator was set at 40 kV and 40 mA. The patterns were recorded

in 2θ ranging from 10 to 100° with a step size of 0.02° and a scan speed of 0.5 s by a repetition mode for 12 h until maximization of the signal-to-noise ratio. The XRD data were analyzed with the MAUD software according to the Rietveld method.

The film thickness and residual porosity were estimated by an α-SE Wollam spectroscopic ellipsometry using a Bruggeman effective medium approximation fitting model with two components:[24] void and Cauchy film.[25] The refractive index parameters for the Cauchy film model were measured on reference samples treated at 450 °C, made by pure and graphene-doped titania, respectively, and not containing the templating agent. Plots of Ψ and Δ as a function of incident wavelength from 400 and 900 nm were simulated using "CompleteEASE v. 4.2" program from Wollam. The results of the fits were evaluated on the basis of the mean squared error (MSE), which was maintained below 30.

A white-light optical profiler (ADE-Shift MicroXAM) with a 50× objective was employed for estimating the thickness of the patterns before and after thermal treatment. Optical properties were measured by a Nicolet Evolution 300 UV−vis spectrophotometer and silica glass was used as background reference.

Photocatalytic Activity Measurements. A solution of stearic acid (100 μL) in ethanol was spin-coated on the nanocomposite titania films by applying a speed rate of 1500 rpm for 30 s. The samples were then placed for increasing times (15, 30, 45, 60, and 75 min) under a UV lamp (λ_{ex} = 365 nm, nominal power density of 470 $\mu W\ cm^{-2}$ at 15 cm) at a distance of 0.5 cm. The experiment of photocatalysis with stearic acid has been reproduced eight times with different samples to test the reproducibility of the performances.

■ RESULTS AND DISCUSSION

We have designed our synthesis keeping in mind some specific features for the final material: aggregate-free dispersion of graphene sheets with low amount of defects, order of the mesostructure, optical transparency, and integration with top-down processing.

The most diffused method for producing graphene in the liquid phase is the chemical modification of graphite in acidic conditions to obtain the so-called graphene oxide (GO). After dispersion in the form of nanosheets, GO can be chemically reduced to partially restore the pristine structure and produce reduced graphene oxide (RGO). However, despite oxidation appearing as a convenient and easy-scalable method to produce exfoliation from graphite, this route presents a main disadvantage: a higher amount of defects due to incomplete reduction of the oxidized carbon structure. To obtain a graphene dispersion, therefore, we have adopted an alternative method which uses ultrasonication to exfoliate graphite immersed in suitable media. This procedure, followed by repetitive centrifugation and sedimentation steps, allows isolating in solution thin platelets formed by single- or few-layer graphene sheets. The first attempt along this way produced colloidal solutions containing very poor graphene concentrations, in the range of 0.01 mg·mL^{-1}; however, more recent developments of the method have allowed reaching remarkable concentrations in the range of several mg·mL^{-1} of graphene.[26] Although the exfoliated graphene (EG) cannot be strictly compared to pristine graphene obtained by mechanical cleavage, it contains a much lower amount of defects in its sp^2-hybridized carbon structure and has recently shown a higher photocatalytic activity than the RGO for the reduction of CO_2 and CH_4 under visible light.[14]

Another important requirement is the possibility of performing a one-pot synthesis, which needs to mix the EG dispersions in the film precursor sol. However, the extreme sensitivity to the chemical environment of the EG dispersions hampers the

direct addition into sols; small changes in the polarity of the solution cause, in fact, reaggregation of the graphene layers into large fragments.

To introduce the exfoliated graphene sheets into the titania mesoporous films, we have used a highly acidic sol, such as those obtained from sol−gel chloride precursors; a colloidal dispersion of graphene in 1-vinyl-2-pyrrolidone (NVP) has been directly mixed to the titania precursor sol containing Pluronic F127 (templating agent), water, and ethanol to produce a homogeneous solution. Mesoporous nanocomposites with ordered porosity have been easily obtained via spin-coating or dip-coating, controlling the relative humidity during deposition. By evaporation-induced self-assembly (EISA), the block copolymers self-organize, producing an ordered array of micelles at the nanoscale.

The thermal treatment is a crucial step in the nanocomposite processing that requires the removal of surfactant and the crystallization of titania into nanosized anatase, avoiding oxidation of graphene sheets and loss in mesopore organization. We have therefore fulfilled all these requirements by a controlled thermal treatment in argon; mesoporous crystalline films obtained by this procedure have shown one of the highest levels of pore organization reported so far.

Structural Characterization of the Graphene Mesoporous Nanocomposite. The chemical and physical changes in the nanocomposite structure have been carefully monitored during each synthetic step. Since the effect of the NVP monomer on the self-assembly kinetics of titania sols has not yet been reported, a systematic investigation of the influence of the graphene solution has been performed. The volume of the graphene dispersion in the sol has been varied from 0 up to 10% without observing a significant sedimentation of the graphene sheets within 10 h (Supporting Information, Figure S1). The influence of graphene colloidal dispersions on the pore organization of the nanocomposites films has been evaluated by grazing incidence small-angle X-ray scattering (GISAXS).[27,28] Figure 1 shows the evolution of the d-spacing relative to the (101) spot in the GISAXS patterns of the graphene mesoporous nanocomposites as a function of the graphene−NVP volume fraction. The GISAXS patterns (inset of the Figure 1 and Figure S2) have been obtained from mesostructured ordered films prepared by spin-coating after treatment at 100 °C. Between 0 and 2.5% in volume, the titania
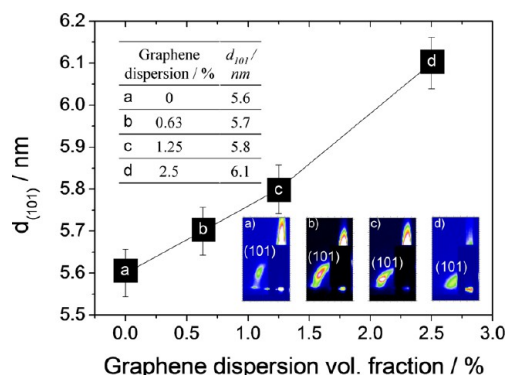

Graphene dispersion / %	d_{101}/ nm
a	0	5.6
b	0.63	5.7
c	1.25	5.8
d	2.5	6.1

Figure 1. Evolution of the d-spacing of the (101) spot in the GISAXS patterns of the graphene mesoporous nanocomposites as a function of the graphene−NVP volume fraction. The films have been treated at 100 °C before measurements and showed an average thickness of 280 nm. The data and the GISAXS patterns are reported as an inset.

797

dx.doi.org/10.1021/am4027407 | ACS Appl. Mater. Interfaces 2014, 6, 795−802

films show the typical (101) spots due to the scattering of a body-centered cubic mesostructure ($Im\bar{3}m$ space group) with the [110] perpendicular to the substrate.[29] However, within this compositional range, we have observed a linear increase of the $d_{(101)}$-spacing (Figure 1) and a decrease in the intensity spot which is caused by the insertion of graphene and polymers into the inorganic organized matrix. A further increase of graphene dispersion up to 5% causes the complete loss of organization with the appearance of a diffuse faint halo in the GISAXS pattern (not shown). The solution based on the 2.5% volume of EG dispersion has been chosen as the best compromise between graphene loading and mesoporous order.

The pore organization has been checked by transmission electron microscopy (TEM); Figure 2a,b reveals the simulta-
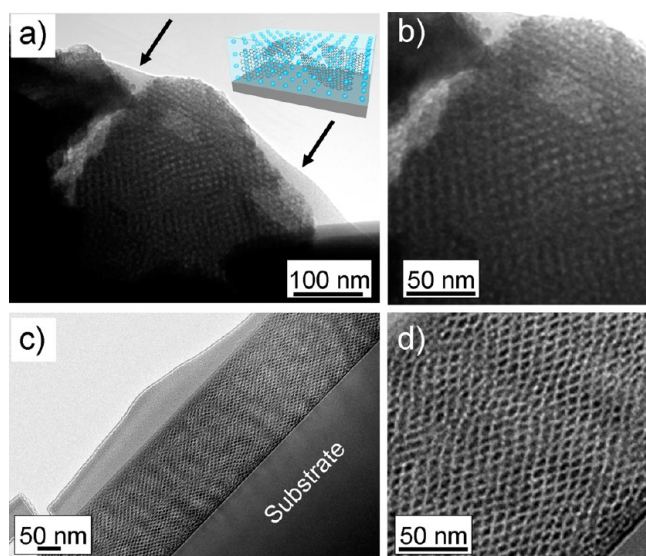

Figure 2. TEM images of representative areas taken from mesoporous graphene−titania nanocomposite films (2.5 vol % of EG dispersion). (a,b) Film fragments before calcination (thickness ≈ 280 nm); arrows indicate the graphene sheets. (c,d) Cross-section dark-field TEM images of the films after calcination.

neous presence of graphene layers (indicated by arrows) and a highly ordered mesoporous titania structure for as-prepared films. The presence of graphene is homogeneously detected in the film and does not affect the organization. Although an unambiguous attribution of the pore symmetry cannot be provided only by TEM characterization, the pore organization appears close-packed cubic, in agreement with the space group symmetry identified by GISAXS measurements. The thermal treatment does not affect the pore order even after titania crystallization; this has been investigated in more detail by cross-section TEM.[30] Figure 2c,d shows the flawless pore organization of the films. From plot profile analysis of the images, the dimension of the elliptical pores has been evaluated as 6.4 ± 1.4 nm for the major axis and 3.8 ± 0.8 nm for the minor axis. Such level of pore organization in titania crystalline films is among the highest reported so far; in fact, the crystallization of the pore walls into anatase usually affects the periodicity, and a loss of order is generally observed. The maintenance of the pore organization even after the thermal treatment is attributed to a delayed removal of the template scaffold from the porous structure. Typically, block copolymers thermally degrade at temperature lower than 350 °C;[31] however, under argon, the thermal degradation is strongly

slowed because of the oxygen deficiency. This allows preservation of the template scaffold even after thermal treatments higher than 350 °C when nucleation and growth of the anatase phase occur.[32]

The crystallinity and composition of the material have been cross-checked using X-ray diffraction (XRD) and TEM. The crystalline structure of the inorganic matrix can be deduced by comparing the bright- and dark-field images of a film fragment (Figure 3a,b) and image analysis allowed estimating the
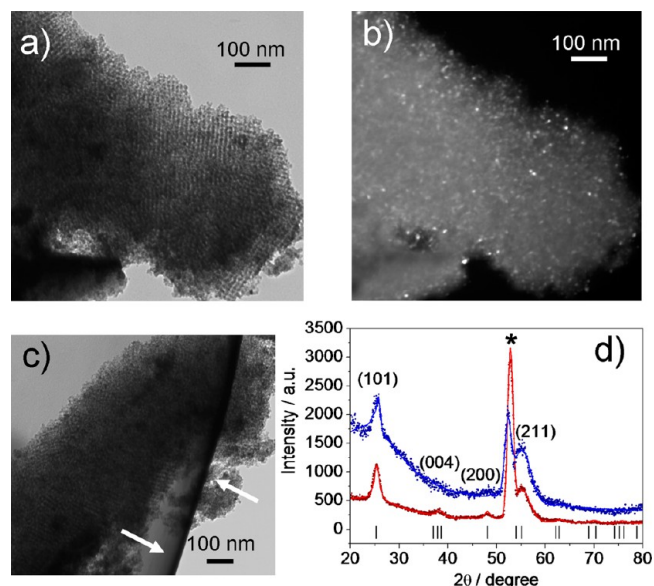

Figure 3. (a−c) Bright- and dark-field TEM images of representative areas taken from graphene mesoporous nanocomposite films after thermal treatment (2.5 vol % of EG dispersion, thickness ≈ 150 nm). The arrows indicate the graphene sheets. (d) XRD patterns of pure titania (red line and wine dots) and graphene-doped titania (2.5 vol % of EG dispersion, blue line and dark blue dots) films after calcination. The dotted lines are the experimental data, and the solid lines are obtained by Rietveld refinement. The most intense diffraction peaks are indexed according to the TiO_2 anatase phase (black ticks). The asterisk indicates the (311) peak of the Si substrate.

crystallite size as 7.8 ± 0.4 nm. Graphene layers are still visible inside film fragments (Figure 3c), confirming that the thermal treatment does not induce degradation on the nanocomposite loading. For XRD measurements, pure and graphene-doped mesoporous titania materials have been compared to study the effect eventually produced by graphene doping (Figure 3d). The two samples show a similar crystalline structure with the appearance of the (101) peak of the anatase phase; an 8 nm crystal size has been estimated by Rietveld refinement. Spectroscopic ellipsometry has been used to determine the film thickness before and after firing; after calcination, fresh coatings with an average thickness of 340 nm shrink down to ~150 nm, both in the case of pure and graphene-loaded mesoporous titania films. The percentage residual porosity after thermal treatment at 450 °C has been also evaluated as 60 ± 3%. Within the error bar, no difference between pure and graphene-loaded mesoporous titania film has been observed.

Figure 4a shows the Raman spectrum of the nanocomposites before thermal treatment (≈340 nm thick) in the range of the 2D band which peaks around 2700 cm^{-1}. This band, which originates from the intervalley scattering of two in-plane transverse optical phonons, provides unambiguous information
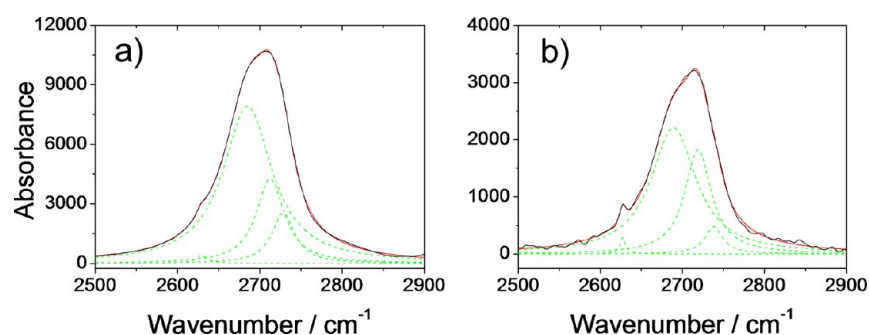
Figure 4. Raman spectra of the 2D band measured on graphene mesoporous nanocomposite films (2.5 vol % of EG dispersion) before and after thermal treatment (a,b). The film thicknesses are around 340 and 150 nm, respectively. The line colors indicate experimental curve (solid black lines), global fit (solid red lines), single Laurentian fit curves (green dotted lines).
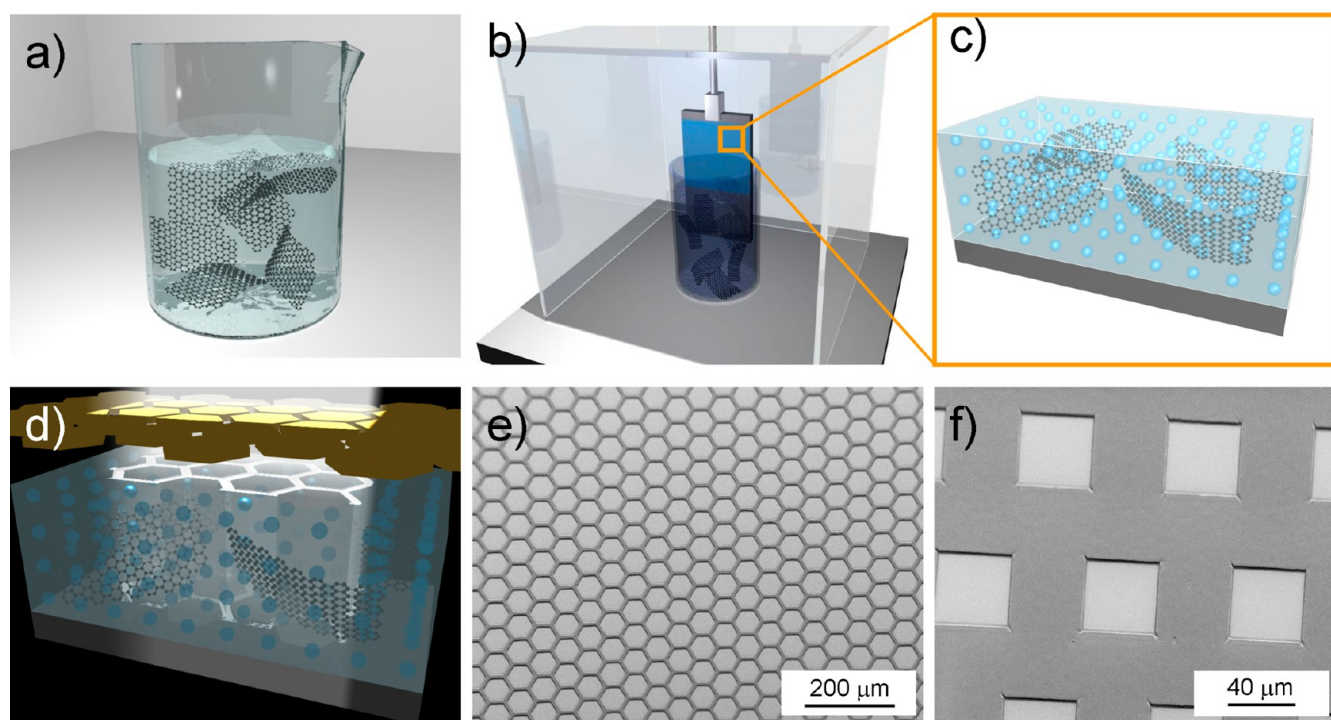

Figure 5. Scheme of the bottom-up, top-down integrated route for microfabrication of nanocomposite mesoporous titania−graphene patterns. (a) Highly acidic titania sol is loaded with graphene dispersion; (b) thin films are produced by dip- or spin-coating; (c) self-assembly process is not affected by graphene, and highly ordered mesoporous titania films are formed. (d) After deposition, thick films (thickness ≈ 800 nm) are patterned by deep X-ray lithography through a mask to obtain micrometer-sized patterns (SEM images, panels e and f).

about the number of constituent graphene layers.[33] In fact, the number of graphene sheets aggregated in the form of platelets controls the number of Lorentzian curves which are experimentally required to fit the Raman band. The best fit of the spectra is obtained using four curves, indicating the presence of graphene bilayers.[34]

The thermal treatment of the coatings has been performed to make the organized porosity fully accessible and to crystallize the inorganic framework into anatase, avoiding thermal degradation or reaggregation of graphene. After thermal treatment, the samples (≈150 nm thick) have been measured again by Raman spectroscopy (Figure 4b). This analysis does not show substantial differences if compared to the Raman investigation on the as-deposited films, confirming that the synthetic protocol is optimized for the fabrication of graphene mesoporous nanocomposites. To exclude that graphene layers are present only on the film surface, the calcined samples have been treated by ultrasonication in ethanol for 5 min, after which

the films have been analyzed again with Raman spectroscopy. No differences in the Raman bands have been detected by comparing the spectra before and after ultrasonication.

Top-down Processing of Nanocomposite Films. Remarkably, the mesoporous titania−graphene films can be easily processed by lithographic techniques before thermal treatment for the production of functional patterns; this allows an integration of the bottom-up film preparation by soft chemistry with the top-down physical patterning. We have used deep X-ray lithography as a versatile tool for obtaining micrometer-sized functional coatings.[35,36] The processing steps are shown in Figure 5; a colloidal suspension of graphene in 1-vinyl-2-pyrrolidone (NVP) is directly added into a titania precursor sol (Figure 5a). Then, mesostructure ordered nanocomposites are easily obtained via spin- or dip-coating, controlling the relative humidity during deposition (Figure 5b). During solvent evaporation, the block copolymer self-assembled, producing an ordered array of micelles at the
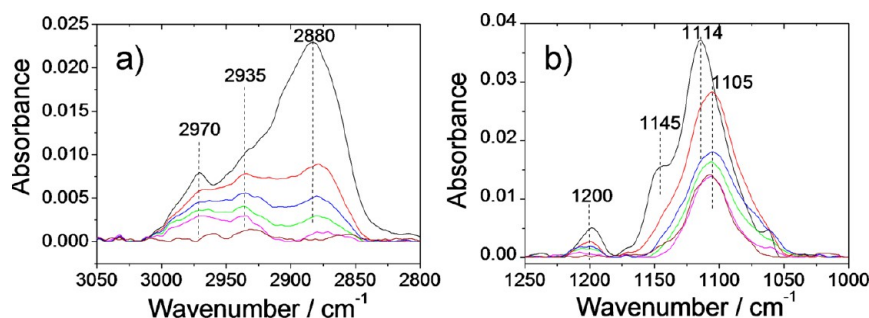
Figure 6. (a,b) FTIR spectra of the graphene mesoporous nanocomposites (2.5 vol % of EG dispersion) exposed at increasing X-ray doses (initial thickness ≈ 340 nm) and finally thermally treated (final thickness ≈ 150 nm). The line colors indicate the following treatments: as-deposited (black line), 275 J cm^{-2} exposure (red line), 550 J cm^{-2} exposure (blue line), 1100 J cm^{-2} exposure (green line), and 2200 J cm^{-2} exposure (magenta line); 2200 J cm^{-2} exposure and treated at 450 °C (wine line). The most intense bands have been marked as a guide for the reader.

nanoscale (Figure 5c). Immediately after drying, the films are exposed to hard X-rays provided by a synchrotron storage ring, through a gold-coated mask (Figure 5d). After exposure, the patterns are developed by immersing the films into an ethanol-based solution for a few minutes and measured by scanning electron microscopy. To test the DXRL performances, the pattering process has been applied to films with different thickness, from 200 nm up to 1 μm thick, obtaining sharp patterns made by nanocomposite mesoporous materials. The results of patterning are shown in the panels e and f of Figure 5, where sharp hexagonal and squared micrometer-shaped arrays have been precisely fabricated on ≈800 nm thick films.

The X-ray exposure induces formation of radicals within the matrix, and this effect plays an important role for the in situ formation of the nanocomposite and functional structure.[37−39] To study the effect of hard X-rays on freshly deposited thin films (∼340 nm), an increasing X-ray dose has been applied to the samples. FTIR spectra of Figure 6a,b show how the lithographic process affects the nanocomposite structure by promoting the densification of the inorganic network and removing the organic templating agent from the films. The degradation of block copolymer and NVP is confirmed by the decrease of the three different bands between 3010 and 2800 cm^{-1} attributed to −CH$_3$ asymmetric, −CH$_2$ asymmetric, and −CH$_3$ symmetric stretching modes, respectively (Figure 6a). A similar decreasing trend has been also observed in the band peak at 1200 cm^{-1}, where we observed the most intense absorption bands of the two organic compounds (Figure 6b). The bands attributed to block copolymers and NVP almost disappear at the highest exposure dose, ensuring an efficient pore opening. After thermal treatment, only a small absorption band peaked at 1105 cm^{-1}, due to the silica of the substrates, remains on the spectra.

After etching and thermal treatment, a "chemical picture" of the pattern has been taken by sampling a submillimeter area with confocal Raman microscopy and integrating the spectra in the 2D band range. The results are shown in Figure 7a,b, where the optical and the chemical images are shown; the correspondence between the optical image and the Raman mapping shows that the development process is effective and completely removes the unexposed parts of the film. At the same time, the analysis confirms that the graphene layers remain homogeneously distributed into the patterns, even after material processing.

Functional Properties of the Graphene Mesoporous Nanocomposites. The careful design of the materials at the nanometric scale allows maximizing the functional properties of
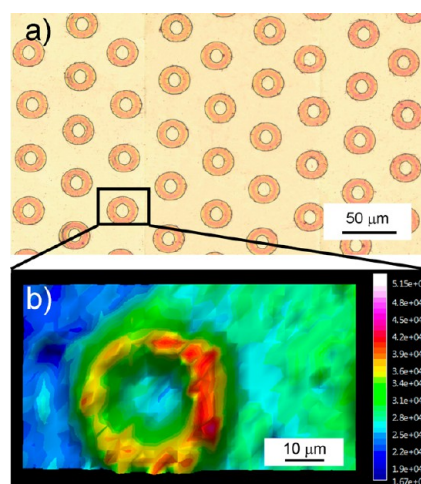

Figure 7. (a) Optical appearance of the functional patterns after thermal treatment (final thickness ≈ 150 nm). (b) Raman mapping obtained from a patterned film exposed to a dose of 1100 kJ cm^{-2} and then developed. The chemical image, reported in false color scale, has been obtained by integration of the graphene 2D band (2.5 vol % of EG dispersion).

the patterned coatings. Thanks to a controlled processing, our method allows for the straightforward fabrication of mesoporous nanocomposites which are highly transparent even after patterning and calcination. For 150 nm thin films, the UV−vis spectrum shows a 90% of transmittance at 500 nm (Figure 8a). In addition, the results of the functional properties of the mesoporous graphene nanocomposites strongly improved. As a proof of concept, the photocatalytic activity of the material has been tested by monitoring the degradation of stearic acid by FTIR after deposition on spin-coated thin films (∼150 nm of thickness). The ratio between the integrals of the bands in the 3010−2800 cm^{-1} range before and after UV exposure has been used as a benchmark for evaluating the kinetics of photo-degradation (Figure 8b). We have observed a remarkable difference in the photoactivity of pure and graphene-doped titania samples; after a 45 min UV exposure, 65% of the stearic acid has been degraded in the pure titania in comparison to 85% in the graphene-doped TiO$_2$ patterns.

This difference corresponds to 30% relative improvement of the photocatalytic activity. A similar value can be also deduced by fitting the stearic acid degradation to pseudo-first-order kinetics (inset of Figure 8b); the rate constants of the reaction when stearic acid is deposited on pure mesoporous and
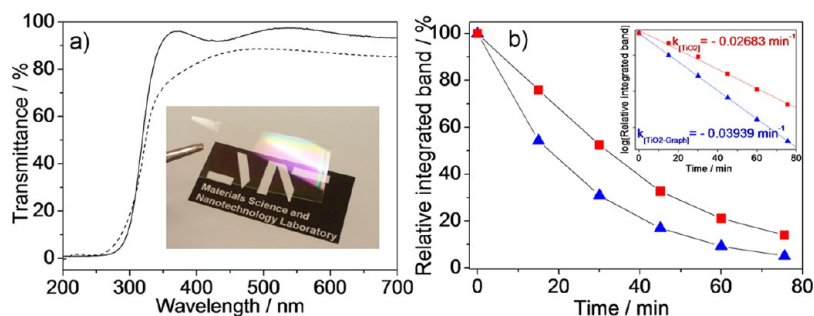
Figure 8. (a) UV−vis spectroscopy of graphene mesoporous nanocomposite films before (solid line) and after (dotted line) thermal calcination (thicknesses ≈340 and 150 nm, respectively). Inset: picture of the film after thermal treatment. (b) Kinetics of photodegration of stearic acid deposited on pure titania (red squares) and graphene−titania (blue triangles) mesoporous nanocomposites (2.5 vol % of EG dispersion). Inset shows the pseudo-first-order fit of stearic acid decay at increasing time of UV excitation.

graphene-doped TiO_2 are -0.02683 ± 0.00100 and -0.03939 ± 0.00018 min^{-1} respectively. The experiments have been reproduced several times using an undoped titania sample as a reference to be sure that the photocatalytic activity was not due to uncontrolled effects. Photocatalytic activity measurements have been performed on both patterned and nonpatterned films with similar thickness after treatment at 450 °C. The photocatalytic activity provided similar results in both cases.

The measured photocatalytic activity is remarkably high, especially if we consider the high transmittance in the visible range presented by the thin coatings. Because of the high degree of pore organization, no larger pores have been necessary to achieve a complete photodegradation of the benchmark molecules in a short time (80 min). We attribute this effect to an exceptional synergic effect of dopant and mesoporous matrix organization. The use of EG with lower concentration of defects provides enhanced catalytic properties, and the highly ordered porosity of the nanocomposites ensures a fast diffusion of the stearic acid inside the films. In fact, the photocatalytic decomposition on titania coatings requires a limited distance between the titania surface and the molecules to be degraded. This is due to the high reactivity of the water radical species produced during the photocatalytic properties. Previous studies attributed a low photocatalytic activity of pure mesoporous titania films to a lack of mass accessing the pores from the surface.[16] With respect to simpler sponge-like structures,[40−42] our porous organized architecture allows for a higher diffusivity, which enables a higher diffusion efficiency of nondegraded molecules toward the titania pore surface. Moreover, worm-like mesoporous structure has shown to reduce the diffusivity inside a mesoporous matrix compared to higher organized porous structures.[43] It has been observed, in fact, that the close-packed cubic ordered structures show the highest diffusivity in comparison to other mesoporous structures with different symmetry or lower degree of order.[44−46] The improved diffusivity also explains the higher photodegradation constant rate provided by the graphene-doped porous and organized titania films in comparison to previous studies.[16] In fact, the pure mesoporous organized film has shown a rate constant 4 times higher than that reported by Du et al., and this value increases by 50% when graphene doping is applied.

CONCLUSIONS

Crystalline ordered mesoporous titania films with a high level of organization have been used as a matrix for the insertion of exfoliated graphene sheets through a one-pot synthesis. The graphene is well-dispersed, and the film does not lose its cubic ordered mesoporous structure after thermal treatment. The films retain a high optical transparency and can be integrated in a bottom-up and top-down process; well-defined and sharp patterns in films with a thickness up to 1 μm have been obtained by deep X-ray lithography. The films show an enhanced photocatalytic activity which is due to three specific contributions: the insertion of exfoliated graphene with a minimized amount of defects, the formation of TiO_2 anatase nanocrystals with photocatalytic properties, and the highly organized mesoporosity with a cubic symmetry which enhances the diffusivity inside the matrix.

A scalable and straightforward synthesis is now available for the preparation of photocatalytic nanocomposite devices based on thin transparent films. Such a protocol can be successfully exploited for the microfabrication of new integrated devices, such as dye-sensitized solar cells and optical limiting devices, which will take advantage of the functional properties of graphene mesoporous nanocomposites.

ASSOCIATED CONTENT

Ⓢ Supporting Information
Table resuming the difference among the samples used for characterizations; graphene dispersion volumetric fraction, thermal treatment, film thickness, and type of substrate (Table ST1). Optical appearance of graphene-doped titania sol for self-assembled mesoporous films as a function of the graphene−NVP volume fraction (Figure S1). GISAXS patterns of the graphene-doped titania film doped with increasing volume fraction of graphene−NVP dispersion (Figure S2). This material is available free of charge via the Internet at http://pubs.acs.org.

AUTHOR INFORMATION

Corresponding Authors
*E-mail: plinio@uniss.it.
*E-mail: luca.malfatti@uniss.it.

Notes
The authors declare no competing financial interest.

ACKNOWLEDGMENTS

■ REFERENCES

(1) Woan, K.; Pyrgiotakis, G.; Sigmund, W. *Adv. Mater.* **2009**, *21*, 2233−2239.

(2) Tu, W.; Zhou, Y.; Zou, Z. *Adv. Funct. Mater.* **2012**, *22*, 1215−1221.

(3) Yang, S.; Feng, X.; Mullen, K. *Adv. Mater.* **2011**, *23*, 3575−3579.

(4) Cao, H.; Li, B.; Zhang, J.; Lian, F.; Kong, X.; Qu, M. *J. Mater. Chem.* **2012**, *22*, 9759−9766.

(5) Zhang, X.; Kumar, P. S.; Aravindan, V.; Liu, H. H.; Sundaramurthy, J.; Mhaisalker, S. G.; Duong, H. M.; Ramakrishna, S.; Madhavi, S. *J. Phys. Chem. C* **2012**, *116*, 14780−14788.

(6) Rafiee, M. A.; Rafiee, J.; Wang, Z.; Song, H.; Yu, Z.-Z.; Koratkar, N. *ACS Nano* **2009**, *3*, 3884−3890.

(7) Tang, L. A.; Wang, J.; Lim, T. K.; Bi, X.; Lee, W. C.; Lin, Q.; Chang, Y. T.; Lim, C. T.; Loh, K. P. *Anal. Chem.* **2012**, *84*, 6693−6700.

(8) Fan, Y.; Huang, K.-J.; Niu, D.-J.; Yang, C.-P.; Jing, Q.-S. *Electrochim. Acta* **2011**, *56*, 4685−4690.

(9) Du, A.; Ng, Y. H.; Bell, N. J.; Zhu, Z.; Amal, R.; Smith, S. C. *J. Phys. Chem. Lett.* **2011**, *2*, 894−899.

(10) Stefik, M.; Yum, J.-H.; Hu, Y.; Graetzel, M. *J. Mater. Chem. A* **2013**, *1*, 4982−4987.

(11) Ng, Y. H.; Lightcap, I. V.; Goodwin, K.; Matsumura, M.; Kamat, P. V. *J. Phys. Chem. Lett.* **2010**, *1*, 2222−2227.

(12) Štengl, V.; Popelková, D.; Vláčil, P. *J. Phys. Chem. C* **2011**, *115*, 25209−25218.

(13) Zhang, H.; Lv, X.; Li, Y.; Wang, Y.; Li, J. *ACS Nano* **2010**, *4*, 380−386.

(14) Liang, Y. T.; Vijayan, B. K.; Gray, K. A.; Hersam, M. C. *Nano Lett.* **2011**, *11*, 2865−2870.

(15) Geng, W.; Liu, H.; Yao, X. *Phys. Chem. Chem. Phys.* **2013**, *15*, 6025−6033.

(16) Du, J.; Lai, X.; Yang, N.; Zhai, J.; Kisailus, D.; Su, F.; Wang, D.; Jiang, L. *ACS Nano* **2010**, *5*, 590−596.

(17) Ganesan, R.; Dumond, J.; Saifullah, M. S. M.; Lim, S. H.; Hussain, H.; Low, H. Y. *ACS Nano* **2012**, *6*, 1494−1502.

(18) Falcaro, P.; Costacurta, S.; Malfatti, L.; Takahashi, M.; Kidchob, T.; Casula, M. F.; Piccinini, M.; Marcelli, A.; Marmiroli, B.; Amenitsch, H.; Schiavuta, P.; Innocenzi, P. *Adv. Mater.* **2008**, *20*, 1864−1869.

(19) DXRL Beam shape specification; http://www.elettra.trieste.it/lightsources/elettra/elettra-beamlines/dxrl/specification.html (accessed July 27, 2013).

(20) Renaud, G. A.; Lazzari, R. B.; Leroy, F. C. *Surf. Sci. Rep.* **2009**, *64*, 255−380.

(21) Müller-Buschbaum, P. *Anal. Bioanal. Chem.* **2003**, *376*, 3−10.

(22) Amenitsch, H.; Bernstorff, S.; Laggner, P. *Rev. Sci. Instrum.* **1995**, *66*, 1624−1626.

(23) Amenitsch, H.; Bernstorff, S.; Kriechbaum, M.; Lombardo, D.; Mio, H.; Rappolt, M.; Laggner, P. *J. Appl. Crystallogr.* **1997**, *30*, 872−876.

(24) For a two-component porous material, the refractive index in the Bruggemann approximation is expressed as $f_v[(n_v^2 - n^2)/(n_v^2 + 2n^2)] + f_m[(n_m^2 - n^2)/(n_m^2 + 2n^2)])0$ where fv, n_v and f_m, n_m are the volume fractions and the refractive index of the pore's void and the bulk material, respectively.

(25) The Cauchy dispersion equation, $n(\lambda) = A_n + B_n/\lambda^2 + C_n/\lambda^4$, allows calculating the refractive index as a function of the wavelength. A_n is a parameter related to the average refractive index of the material, whereas B_n and C_n are parameters that provide the shape or curvature of the $n(\lambda)$ curve.

(26) Nuvoli, D.; Valentini, L.; Alzari, V.; Scognamillo, S.; Bittolo Bon, S.; Piccinini, M.; Illescas, J.; Mariani, A. *J. Mater. Chem.* **2011**, *21*, 3428−3431.

(27) Perlich, J.; Kaune, G.; Memesa, M.; Gutmann, J. S.; Müller-Buschbaum, P. *Philos. Trans. R. Soc. A* **2009**, *367*, 1783−1798.

(28) Rawolle, M.; Ruderer, M. A.; Prams, S. M.; Zhong, Q.; Magerl, D.; Perlich, J.; Roth, S. V.; Lellig, P.; Gutmann, J. S.; Müller-Buschbaum, P. *Small* **2011**, *7*, 884−891.

(29) Crepaldi, E. L.; Soler-Illia, G. J. J. A.; Grosso, D.; Cagnol, F.; Ribot, F.; Sanchez, C. *J. Am. Chem. Soc.* **2003**, *125*, 9770−9786.

(30) Grosso, D.; Soler-Illia, G. J. J. A.; Crepaldi, E. L.; Cagnol, F.; Sinturel, C.; Bourgeois, A.; Brunet-Bruneau, A.; Amenitsch, H.; Albouy, P. A.; Sanchez, C. *Chem. Mater.* **2003**, *15*, 4562−4570.

(31) Malfatti, L.; Falcaro, P.; Amenitsch, H.; Caramori, S.; Argazzi, R.; Bignozzi, C. A.; Enzo, S.; Maggini, M.; Innocenzi, P. *Microporous Mesoporous Mater.* **2006**, *88*, 304−311.

(32) Innocenzi, P.; Malfatti, L.; Kidchob, T.; Enzo, S.; Della Ventura, G.; Schade, U.; Marcelli, A. *J. Phys. Chem. C* **2010**, *114*, 22385−22391.

(33) Ferrari, A. C. *Solid State Commun.* **2007**, *143*, 47−57.

(34) Malard, L. M.; Pimenta, M. A.; Dresselhaus, G.; Dresselhaus, M. S. *Phys. Rep.* **2009**, *473*, 51−87.

(35) Falcaro, P.; Malfatti, L.; Vaccari, L.; Amenitsch, H.; Marmiroli, B.; Grenci, G.; Innocenzi, P. *Adv. Mater.* **2009**, *21*, 4932−4936.

(36) Falcaro, P.; Malfatti, L.; Innocenzi, P. *Soft Matter* **2012**, *8*, 3722−3729.

(37) Malfatti, L.; Marongiu, D.; Costacurta, S.; Falcaro, P.; Amenitsch, H.; Marmiroli, B.; Grenci, G.; Casula, M. F.; Innocenzi, P. *Chem. Mater.* **2010**, *22*, 2132−2137.

(38) Malfatti, L.; Falcaro, P.; Marmiroli, B.; Amenitsch, H.; Piccinini, M.; Falqui, A.; Innocenzi, P. *Nanoscale* **2011**, *3*, 3760−3766.

(39) Pinna, A.; Lasio, B.; Piccinini, M.; Marmiroli, B.; Amenitsch, H.; Falcaro, P.; Tokudome, Y.; Malfatti, L.; Innocenzi, P. *ACS Appl. Mater. Interfaces* **2013**, *5*, 3168−3175.

(40) Niedermeier, M. A.; Rawolle, M.; Lellig, P.; Körstgens, V.; Herzig, E. M.; Buffet, A.; Roth, S. V.; Gutmann, J. S.; Fröschl, T.; Hüsing, N.; Müller-Buschbaum, P. *ChemPhysChem* **2013**, *14*, 597−602.

(41) Rawolle, M.; Körstgens, V.; Ruderer, M. A.; Metwalli, E.; Guo, S.; Herzog, G.; Benecke, G.; Schwartzkopf, M.; Buffet, A.; Perlich, J.; Roth, S. V.; Müller-Buschbaum, P. *Rev. Sci. Instrum.* **2012**, *83*, 106104.

(42) Niedermeier, M. A.; Magerl, D.; Zhong, Q.; Nathan, A.; Körstgens, V.; Perlich, J.; Roth, S. V.; Müller-Buschbaum, P. *Nanotechnology* **2012**, *23*, 145602.

(43) Zürner, A.; Kirstein, J.; Döblinger, M.; Bräuchle, C.; Bein, T. *Nature* **2007**, *450*, 705−708.

(44) Walcarius, A.; Kuhn, A. *Trends Anal. Chem.* **2008**, *27*, 593−603.

(45) Etienne, M.; Quach, A.; Grosso, D.; Nicole, L.; Sanchez, C.; Walcarius, A. *Chem. Mater.* **2007**, *19*, 844−856.

(46) Wei, T.-C.; Hillhouse, H. W. *Langmuir* **2007**, *23*, 5689−5699.

802

dx.doi.org/10.1021/am4027407 | *ACS Appl. Mater. Interfaces* 2014, 6, 795−802